Design, implementation, and performance evaluation of a 4-DOF parallel robot

Hee-Byoung Choi†*, Atsushi Konno‡ and Masaru Uchiyama‡

† *Mechatronics Engineering, Chungnam National University, 79 Daehangno, Yuseong-gu, Daejeon 305-764, Korea*
‡ *Department of Aerospace Engineering, Tohoku University, Aoba-yama 01, Sendai 980-8579, Japan*

SUMMARY
This paper deals with the design, implementation, and performance evaluation of a new type of 4-DOF parallel mechanism providing three translations and one rotation for high-speed handling and machining. This parallel mechanism is named H4. A necessary condition and system configuration of the H4 are also described. Hardware and kinematics of the H4 is addressed and the manipulability ellipsoid which is one of the widely used methods to examine the design of parallel mechanisms is addressed. The performance evaluation is carried out to demonstrate the H4 robot. The simulation and experimental results show that three different controllers, the PD, PD + velocity feedforward, and dynamic compensation controller, dramatically improve the trajectory tracking accuracy.

KEYWORDS: Design, parallel robot, 4-DOF

1. Introduction
Recently, parallel robots have been studied enthusiastically since their capabilities are superior to those of conventional serial robots in many aspects.[7,15] The notable advantages of the parallel mechanism are high accuracy, high-load capacity, high rigidity, and quickness.

Many kinds of parallel robots have been developed so far.[1,11,16] Clavel developed a novel 3-DOF pantograph-type parallel robot named DELTA.[6] Since the DELTA mechanism has only 3-DOF, applications are limited. The DELTA robot can have 6-DOF if given additional serially actuated 3-DOF for postures. Such serial-parallel hybrid robots have a relatively large workspace for postures, however, at a loss of some of the advantages of parallel mechanisms such as rigidity and quickness. In contrast, Pierrot *et al.* proposed a 6-DOF fully parallel robot HEXA[14,17,18] which has a pantograph mechanism similar to the DELTA robot. J. Kim *et al.* developed Eclipse-II which is an over-actuated 7-DOF parallel mechanism.[9,10]

There are a lot of applications in which 3-DOF are not enough and 6-DOF are too many. For example, 4-DOF (3-DOF for translation and 1-DOF for rotation) are necessary and enough in many pick-and-place tasks which are typical industrial applications. Nevertheless, only few attempts have been made so far on development of 4-DOF parallel robots.

Pierrot *et al.* proposed a 4-DOF parallel mechanism called H4 for such applications .[12,13] The H4 mechanism proposed by Pierrot *et al.* has large workspace and high-speed acceleration along the vertical axis (z-axis), since all of the four motors are mounted on the upper base. However, most of industrial applications require a large workspace and good performance in horizontal plain (x–y plane).

In order to meet the requirement for industrial applications, a new type of H4 robot is developed ("H4" is not a name of a specific robot but a name of a class of 4-DOF parallel mechanisms, therefore, the developed new robot is also called "H4" in this paper).[3] The new H4 robot proposed in this paper equips two motors on an upper base while two other motors are on a side base. Therefore, the performance and dimensions of the workspace along the vertical axis and in the horizontal plane are well balanced. This paper addresses the design, kinematics, manipulability, dynamics, and control of the newly developed 4-DOF parallel robot H4.

2. Hardware Configuration of the Newly Developed H4 Robot
The basic concept of H4 is shown by a simple architectural scheme illustrated in Fig. 1, in which joints are represented by rectangles and links that connect joints are represented by lines. *P*, *R*, *U*, and *S* represent prismatic, revolute, universal, and spherical joint, respectively. A quasi-equivalence exists between *U*–*U* (Universal–Universal) and $(S–S)_2$ (two Spherical–Spherical) chains.[12] For mechanical simplicity, $(S–S)_2$ chain is chosen for the new H4.

2.1. Constraints
The four $(S–S)_2$ chains of the H4 robot are illustrated in Fig. 2. Spherical joints are denoted by "◯". In the structure shown in Fig. 2, $B_{i1}–B_{i2}–C_{i1}–C_{i2}$ ($i = 1 \sim 4$) form parallelograms. Therefore, $\overrightarrow{B_{i1}B_{i2}}$ and $\overrightarrow{C_{i1}C_{i2}}$ are always parallel. Due to these constraints, the vectors $\boldsymbol{v}_1$ and $\boldsymbol{v}_2$ shown in Fig. 2 are kept perpendicular to the ground surface. In other words, the rotations around pitch and roll axes of the traveling plate are constrained, while only the rotation around yaw axis is allowed. Figure 3 shows the developed H4 robot.

2.2. Motors
The robot employs direct-drive motors M-SSB014 manufactured by NSK Ltd. The motor is equipped with a
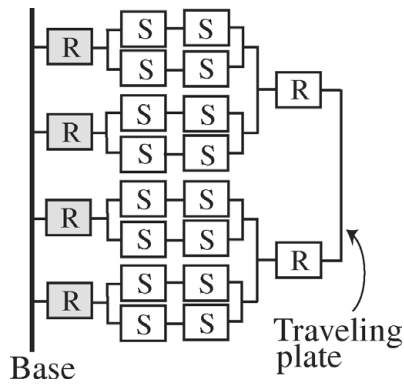
* Corresponding author. E-mail: ojhee@cnu.ac.kr
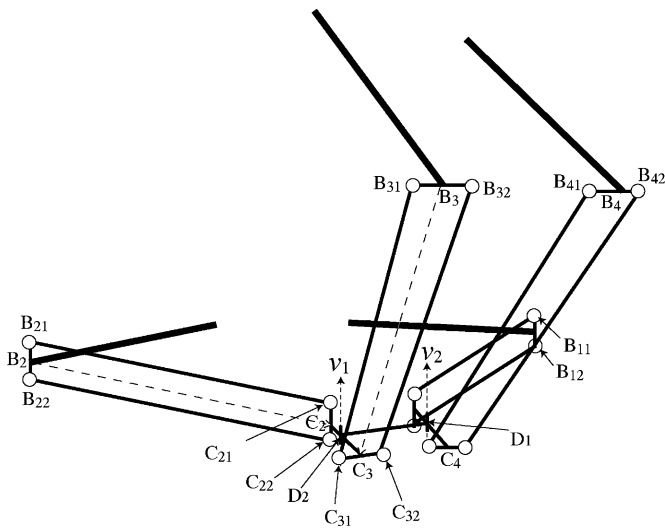
Fig. 1. Architectural scheme of the H4.

Fig. 2. $R(SS)_2$ chains.

resolver to detect the rotation angle. The maximum torque, rated speed, and weight of the motor are 14 Nm, 3.75 rps, and 6 kg, respectively.

2.3. Arms

The arms are made of aluminum square ($0.02\,\text{m} \times 0.02\,\text{m}$) pipes whose thickness is 0.002 m (Fig. 4). The length of the arm is $L = 0.26$ m. The moment of inertia around the rotary axis is $4.527 \times 10^{-3}\,\text{kg}\,\text{m}^2$. The operating range of the arm around the motor axis is limited to 150° by mechanical stoppers made of synthetic resin.

Fig. 3. Newly developed H4 robot.

2.4. Rods

The rods are made of aluminum cylindrical pipes whose outer diameter is 8 mm. The length and thickness of the pipe are $M = 0.48$ m and 0.001 m, respectively (Fig. 5). The total mass of the rod is 0.048 kg.

2.5. Passive spherical joints

As described above, (S–S)$_2$ chains are used instead of (U–U) chains. Spherical joints connect between the arms and rods, and between the rods and traveling plate. The spherical joints (Fig. 6) are newly developed in order to enlarge the movable range of parallel robots.[8] The movable range of the developed spherical joint is $\pm 40°$, while the range of the general off-the-shelf spherical joints is approximately $\pm 20°$.
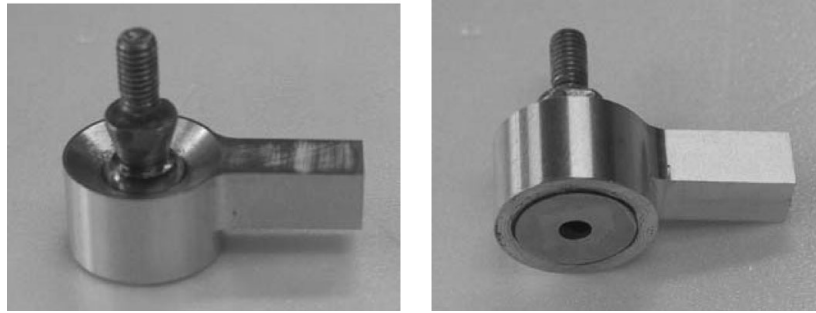

Fig. 4. Arm.

Fig. 5. Rod.

Fig. 6. Newly developed spherical joint whose movable range is $\pm 40°$.

2.6. Traveling plate

The traveling plate is composed of two lateral bars and one central bar (Fig. 7). The difference of translational positions between the two lateral bars rotates the central bar. The two lateral bars are constrained by kinematic chains not to rotate with respect to the base frame, and hence, they are always parallel. The traveling plate is made of aluminum plate and weighs 0.398 kg.

3. Kinematics of the H4

3.1. Geometric description

The parameters L, M, A, and h shown in Fig. 8 are the length of the arm, the length of the rod, the offset of the motor axis from the center of the base, and the offset of each ball-joint from the center of traveling plate, respectively. The points A_i, B_i, and C_i are the intersections between the motor axis and arm, between the arm and rod, and between the rod and traveling plate, respectively. The numbers $i = 1 \sim 4$ are assigned for each serial kinematic chain. The following three coordinate systems are defined here:

- Σ_b: the base coordinate system,
- Σ_t: the traveling plate coordinate system,
- Σ_{ai}: the motor coordinate system fixed on the ith motor so that $z_{ai} = y_b$ ($i = 1, 2$), $z_{ai} = z_b$ ($i = 3, 4$) and y_{ai} is parallel to the rotation axis of the ith motor ($i = 1 \sim 4$).

The parameters h, Q_y, and Q_z (Fig. 8) of the real robot are 0.06 m, 0.42 m, and 0.42 m, respectively.

3.2. Inverse kinematics

As is the case with most parallel robots, the inverse kinematics of H4 is analytically derived. The traveling plate is composed of three parts: two lateral bars and one central bar (Fig. 8). The four corners C_1, C_2, C_3, and C_4 form a parallelogram.

Let ^bC_i, $^{ai}B_i$, and $^{ai}C_i$ be the homogeneous coordinates of the points C_i with respect to Σ_b, B_i with respect to Σ_{ai} and C_i with respect to Σ_{ai}, respectively.

When the point O_t, origin of the traveling plate coordinate system, and the rotation of the central bar of the traveling plate are given by $\boldsymbol{p} = [x \ y \ z \ \alpha]^T$ with respect to Σ_b, the homogeneous coordinates ^bC_i and $^{ai}C_i$ are expressed as follows:

$$
^bC_i(\boldsymbol{p}) = \begin{bmatrix} x + h E_{1i} \cos\alpha \\ y + h E_{1i} \sin\alpha + h E_{2i} \\ z \\ 1 \end{bmatrix} = \begin{bmatrix} ^b\boldsymbol{c}_i \\ 1 \end{bmatrix}, \quad (1)
$$

$E_{11} = E_{14} = 1, \quad E_{12} = E_{13} = -1, \quad E_{21} = E_{22} = 1,$

$E_{23} = E_{24} = -1,$

$$
^{ai}C_i(\boldsymbol{p}) = {}^{ai}T_b\, {}^bC_i = \begin{bmatrix} ^{ai}\lambda_i \\ ^{ai}\rho_i \\ ^{ai}\mu_i \\ 1 \end{bmatrix} = \begin{bmatrix} ^{ai}\boldsymbol{c}_i \\ 1 \end{bmatrix}, \quad (2)
$$

where $^{ai}T_b$ is the constant homogeneous transfer matrix from Σ_b to Σ_{ai}.
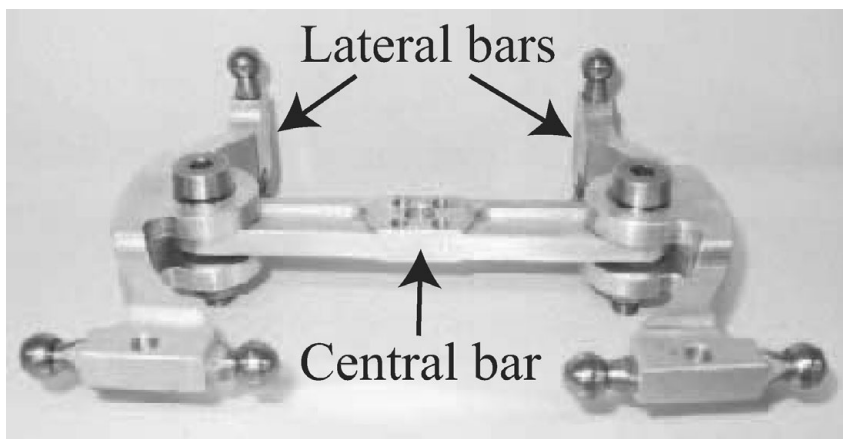

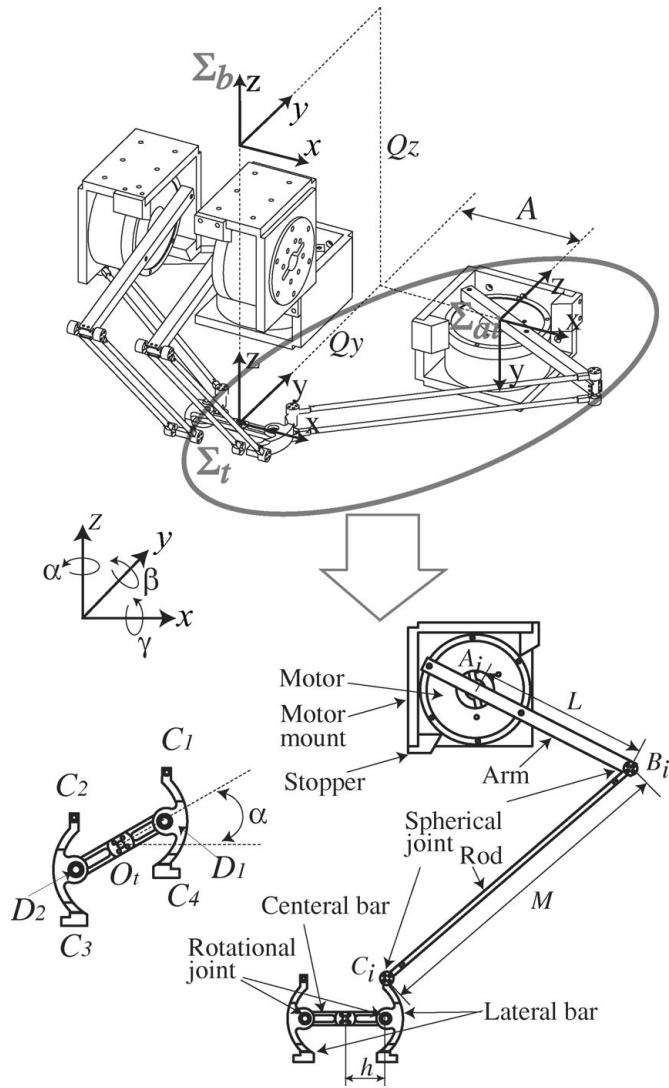Fig. 7. Traveling plate which is composed of two lateral bars and a central bar.

Fig. 8. Coordinate systems and design parameters.

The homogeneous coordinates $^{ai}\boldsymbol{B}_i$ are functions of the motor angle θ_i and expressed as

$$^{ai}\boldsymbol{B}_i(\theta_i) = \begin{bmatrix} L\cos\theta_i \\ 0 \\ -L\sin\theta_i \\ 1 \end{bmatrix} = \begin{bmatrix} ^{ai}\boldsymbol{b}_i \\ 1 \end{bmatrix}. \tag{3}$$

The kinematic closure of each elementary chain is given by:

$$\|\overrightarrow{^{ai}B_i\,^{ai}C_i}\|^2 = \left(^{ai}\boldsymbol{c}_i(\boldsymbol{p}) - ^{ai}\boldsymbol{b}_i(\theta_i)\right)^T \left(^{ai}\boldsymbol{c}_i(\boldsymbol{p}) - ^{ai}\boldsymbol{b}_i(\theta_i)\right)$$
$$= M^2. \tag{4}$$

Substituting Eqs. (2) and (3) into Eq. (4), the motor angles θ_i are given by

$$\theta_i = 2\tan^{-1}\left(\frac{-^{ai}\mu_i \pm \sqrt{^{ai}\mu_i^2 + ^{ai}\lambda_i^2 - W_i^2}}{^{ai}\lambda_i + W_i} \right), \tag{5}$$

where

$$W_i = \frac{L^2 - M^2 + ^{ai}\mu_i^2 + ^{ai}\lambda_i^2 + ^{ai}\rho_i^2}{2L}.$$

The choice of sign in Eq. (5) corresponds to the multiple solution in which we use "elbow-down" solution.

3.3. Forward kinematics
In general, it is not always possible to solve the forward kinematics of a parallel robot analytically. Arai and others proposed a numerical solution of the forward kinematics of a parallel robot utilizing the Newton–Raphson method.[2]

In case of H4, it is not possible to solve the forward kinematics analytically, but possible to solve in a closed form. The forward kinematics solution of the H4 is given by solving a set of four nonlinear simultaneous equations.[4] Please refer ref. [4] for more detail.

3.4. Workspace
The movable region of the arm is illustrated in Fig. 9(a). The workspace of the H4 is presented in Fig. 9(b). Since the overmobility (forward singularity) easily happens when $z \geq -0.42$ m, hence, the workspace is calculated in the region $z < -0.42$ m.[5]

3.5. Jacobian matrices
The homogeneous coordinate $^{ai}\boldsymbol{B}_i$ calculated by Eq. (3) is transferred with respect to the base coordinate system as follows:

$$^b\boldsymbol{B}_i(\theta_i) = {}^b\boldsymbol{T}_{ai}\,^{ai}\boldsymbol{B}_i = \begin{bmatrix} ^b\boldsymbol{b}_i \\ 1 \end{bmatrix}, \tag{6}$$

where $^b\boldsymbol{T}_{ai}$ is the constant homogeneous transfer matrix from Σ_{ai} to Σ_b.

Equation (4) can be rewritten with respect to the base coordinate system Σ_b as follows:

$$f_i(\boldsymbol{p},\,\theta_i) = \frac{1}{2}\|\overrightarrow{B_iC_i}\|^2 - \frac{1}{2}M^2 = 0, \tag{7}$$

where the vector $\overrightarrow{B_iC_i}$ is given by:

$$\overrightarrow{B_iC_i} = {}^b\boldsymbol{c}_i(\boldsymbol{p}) - {}^b\boldsymbol{b}_i(\theta_i).$$

Equation (7) for all i is packed into a single equation as follows:

$$\boldsymbol{f}(\boldsymbol{p},\,\boldsymbol{\theta}) = \boldsymbol{0}. \tag{8}$$

Differentiating Eq. (8) with respect to time, the following relationship is derived:

$$\boldsymbol{J}_p\,\dot{\boldsymbol{p}} + \boldsymbol{J}_\theta\,\dot{\boldsymbol{\theta}} = \boldsymbol{0}, \tag{9}$$

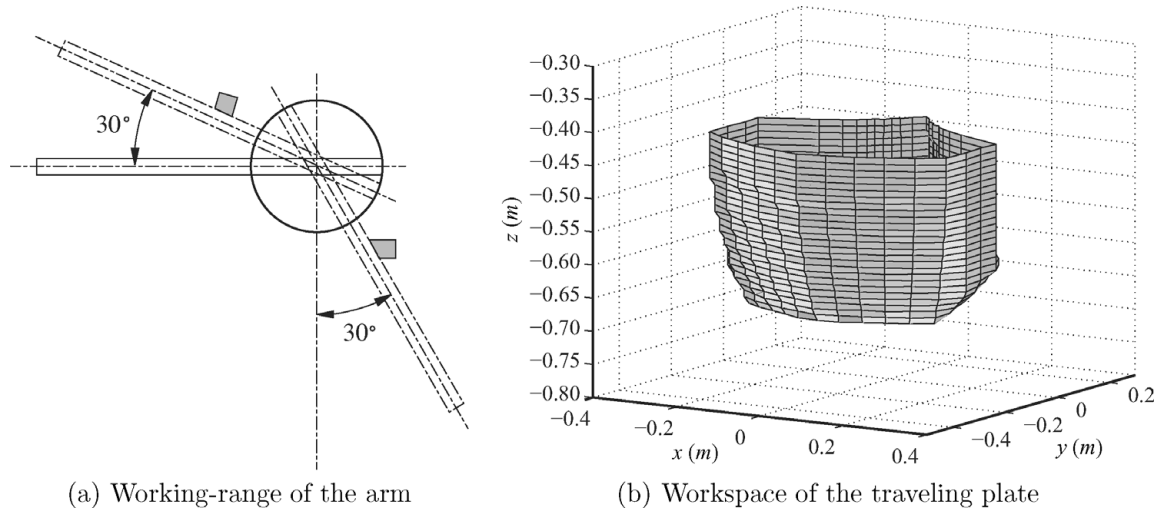(a) Working-range of the arm

(b) Workspace of the traveling plate

Fig. 9. Working range of arm and workspace.

where

$$\boldsymbol{J}_p = \begin{bmatrix} \overrightarrow{B_1C_1} \cdot \dfrac{\partial\,{}^b\boldsymbol{c}_1}{\partial x} & \ldots & \overrightarrow{B_1C_1} \cdot \dfrac{\partial\,{}^b\boldsymbol{c}_1}{\partial \alpha} \\ \vdots & \ldots & \vdots \\ \overrightarrow{B_4C_4} \cdot \dfrac{\partial\,{}^b\boldsymbol{c}_4}{\partial x} & \ldots & \overrightarrow{B_4C_4} \cdot \dfrac{\partial\,{}^b\boldsymbol{c}_4}{\partial \alpha} \end{bmatrix}$$

$$= \begin{bmatrix} \left(\overrightarrow{B_1C_1}\right)^T & \overrightarrow{B_1C_1} \cdot \dfrac{\partial\,{}^b\boldsymbol{c}_1}{\partial \alpha} \\ \vdots & \vdots \\ \left(\overrightarrow{B_4C_4}\right)^T & \overrightarrow{B_4C_4} \cdot \dfrac{\partial\,{}^b\boldsymbol{c}_4}{\partial \alpha} \end{bmatrix},$$

$$\boldsymbol{J}_\theta = -\mathrm{diag}\left[\overrightarrow{B_iC_i} \cdot \dfrac{\partial\,{}^b\boldsymbol{b}_i}{\partial \theta_i}\right].$$

Equation (9) can be rewritten as follows:

$$\dot{\boldsymbol{p}} = -\boldsymbol{J}_p^{-1}\boldsymbol{J}_\theta \dot{\boldsymbol{\theta}} = \boldsymbol{J}\dot{\boldsymbol{\theta}} \tag{10}$$

4. Manipulability

In this section, the manipulability ellipsoid and the manipulability measure of the H4 robot is investigated. It will be beneficial for design and planning of the H4 robot to have a good manipulating ability in positioning and orienting the end effector. The manipulability ellipsoid and the manipulability measure were suggested by refs. [19, 20].

If we consider a manipulator with n DOF whose joint variables are denoted by $\boldsymbol{q}$. A vector of the position and orientation of the end effector are described by $\boldsymbol{p} = [p_1, p_2, \ldots, p_m]^T$ and $\boldsymbol{\theta} = [\theta_1, \theta_2, \ldots, \theta_n]^T$ $(m \leq n)$ is the joint angle vector. Manipulability ellipsoid in task space are transformed from the area in joint velocity space as follows:

$$\|\dot{\boldsymbol{\theta}}\| \equiv \dot{\boldsymbol{\theta}}^T\dot{\boldsymbol{\theta}} \equiv \dot{\boldsymbol{p}}^T\boldsymbol{J}^{+^T}\boldsymbol{J}^+\dot{\boldsymbol{p}} \leq 1, \tag{11}$$

where $\boldsymbol{J}^+$ is pseudo-inverse matrix[19,20] of the Jacobian matrix $\boldsymbol{J}$.

Manipulability measure also has been defined in many previous researches using Jacobian:[19,20]

$$\omega = \sqrt{\det(JJ^T)} = \sigma_1\sigma_2\ldots\sigma_m \tag{12}$$

where σ_i $(i = 1, \ldots, m)$ are singular values of $\boldsymbol{J}$.

4.1. Manipulability of the H4 robot

To show the H4 robot has good performances along x- and y-axis, we calculate manipulability of the H4 robot. Figures 10, 11, and 12 show manipulability ellipsoid along x-, y- and z-axis, respectively. Here, in these figures, the subparts (a), (b), (c), and (d) stand for top view, 3D view, front view, and side view, respectively. Figure 13 shows the value of w as a manipulability measure.

5. A Simplified Dynamic Model of the H4 Robot

A simplified dynamic model which was developed by ref. [14] is introduced in this section. The simplified model assumes that the mass of the rod m_r is concentrated at B_i (see Fig. 14(a)), and the inertia of the rod can be neglected. This assumption greatly contributes to reduce the cost of dynamics calculation, since the dynamics of the rod is not included. Actually, the mass and inertia of the H4 robot are small enough to be neglected.

5.1. Dynamic model of the arm

Force and moment acting on the arm are illustrated in Fig. 14(a). When a force $\boldsymbol{F}_{Bi}$ is applied to B_i through the rod i, the force produces a moment n_i around the motor axis $\boldsymbol{Y}_{ai}$. The force $\boldsymbol{F}_{Bi}$ is generated by the dynamics of the traveling plate. From the principle of virtual work, the moment n_i is related to the forces and moment acting on the traveling plate as follows:

$$\Delta\boldsymbol{\theta}^T\boldsymbol{n} = \Delta\boldsymbol{p}^T\begin{bmatrix}\boldsymbol{F}_t \\ N_{tz}\end{bmatrix}, \tag{13}$$

$$\boldsymbol{n} = \begin{bmatrix}n_1 & n_2 & n_3 & n_4\end{bmatrix}^T,$$

$$\boldsymbol{\theta} = \begin{bmatrix}\theta_1 & \theta_2 & \theta_3 & \theta_4\end{bmatrix}^T,$$
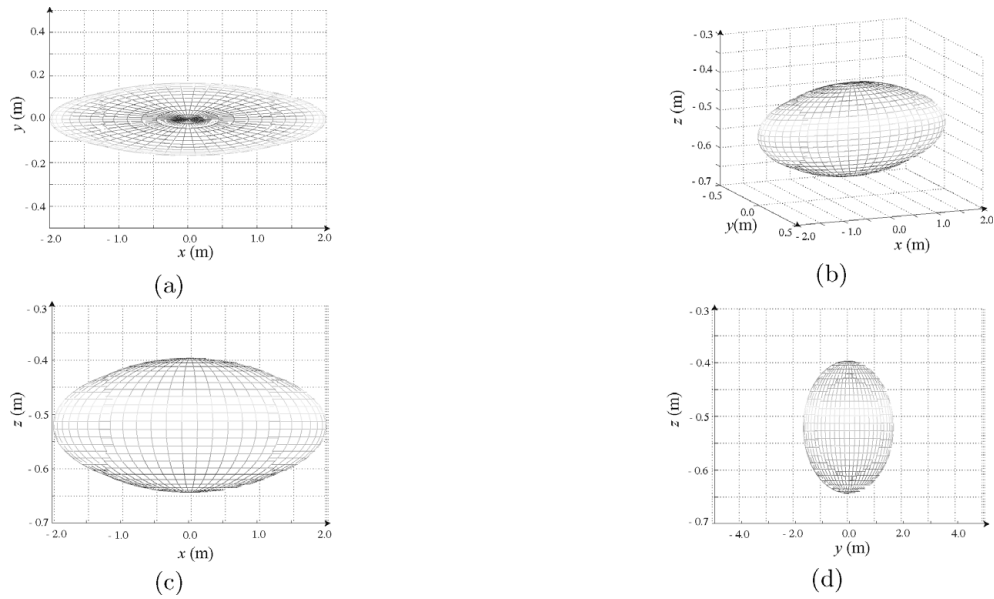
Fig. 10. Manipulability ellipsoid along x-axis at $y = 0$ m and $z = -0.52$ m.

where $\boldsymbol{F}_t$ is the force acting on the traveling plate while N_{tz} is the moment acting on the plate around the Z_t-axis. $\Delta\boldsymbol{\theta}$ and $\Delta\boldsymbol{p}$ are the virtual displacements.

Equation (10) can be rewritten in a difference equation form as follows:

$$\Delta\boldsymbol{p} = \boldsymbol{J}\Delta\boldsymbol{\theta}. \tag{14}$$

Substituting Eq. (14) into Eq. (13), the relationship between $\boldsymbol{F}_t$, N_{tz} and $\boldsymbol{n}$ is given by

$$\boldsymbol{n} = \boldsymbol{J}^T \begin{bmatrix} \boldsymbol{F}_t \\ N_{tz} \end{bmatrix}. \tag{15}$$

Using the simplified model, the dynamic equation is given as follows:

$$\boldsymbol{\tau} = \left(I_a + m_r L^2 + I_m\right) \boldsymbol{I}_{4\times4}\ddot{\boldsymbol{\theta}} + (m_a l_a + m_r L)\,g \begin{bmatrix} 0 \\ 0 \\ \cos\theta_3 \\ \cos\theta_4 \end{bmatrix}$$

$$+ \boldsymbol{V}(\dot{\boldsymbol{\theta}}) + \boldsymbol{J}^T \begin{bmatrix} \boldsymbol{F}_t \\ N_{tz} \end{bmatrix}, \tag{16}$$

where $\boldsymbol{\tau}$ is the joint torque vector, I_m and I_a are the inertias of the motor and arm, respectively, l_a is the length from the

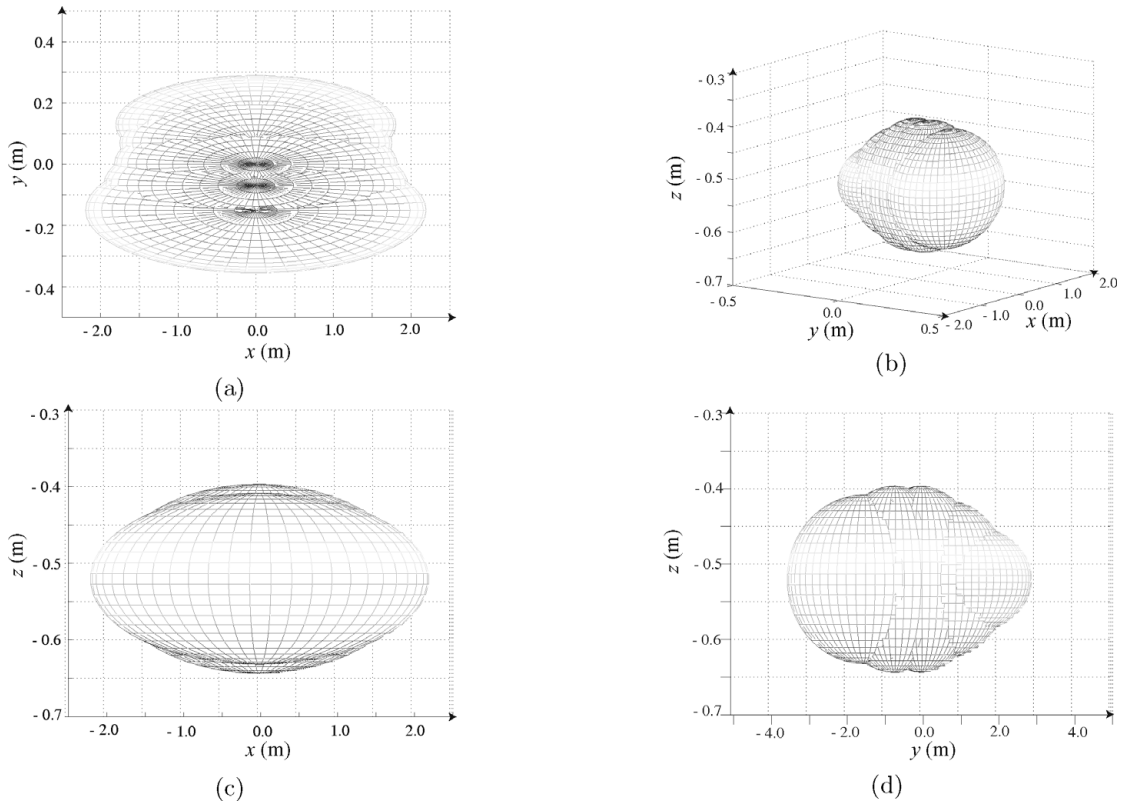Fig. 11. Manipulability ellipsoid along y-axis at $x = 0$ m and $z = -0.52$ m.
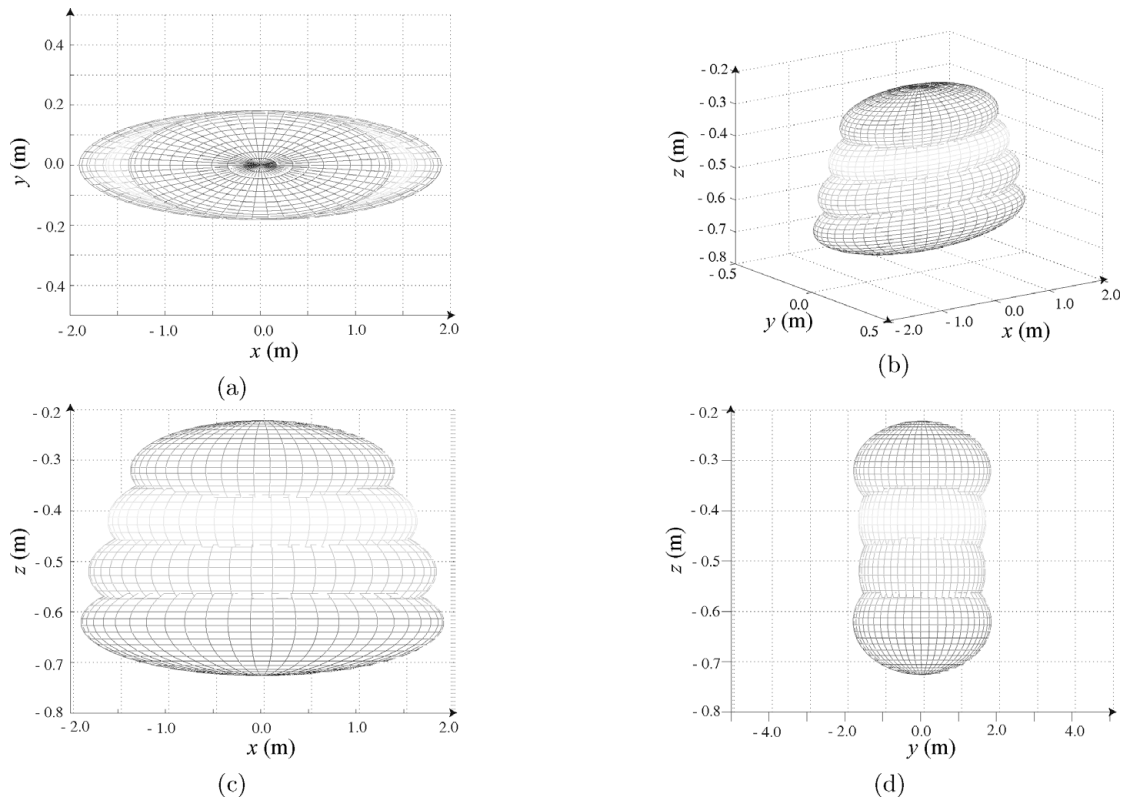
Fig. 12. Manipulability ellipsoid along *z*-axis at $x = 0.0$ m and $y = 0.0$ m.

(a) x=-0.4~0.4 [m], y=0 [m], z=-0.8~-0.2 [m]

(b) x=0.0 [m], y=-0.3~0.2 [m], z=-0.8~-0.2 [m]

Fig. 13. Manipulability measure.

(a) Force and moment generated on the arm

(b) Forces and moments generated on the traveling plate

Fig. 14. A simplified model.

motor axis to the center of mass of the arm (Fig. 14-(a)), g is the gravity acceleration, and $V(\dot{\boldsymbol{\theta}})$ is the viscous frictional moment.

5.2. Dynamics of the traveling plate
Forces and moments acting on the traveling plate are illustrated in Fig. 14-(b). The dynamics of the traveling plate is expressed as follows:

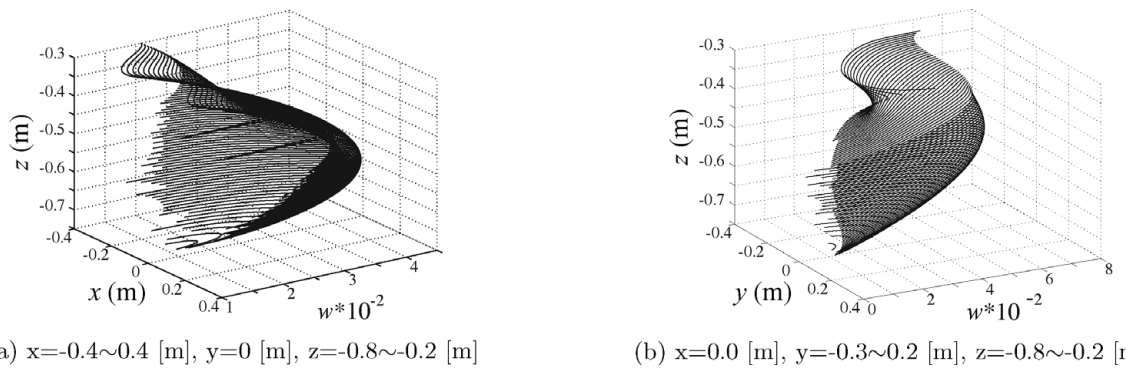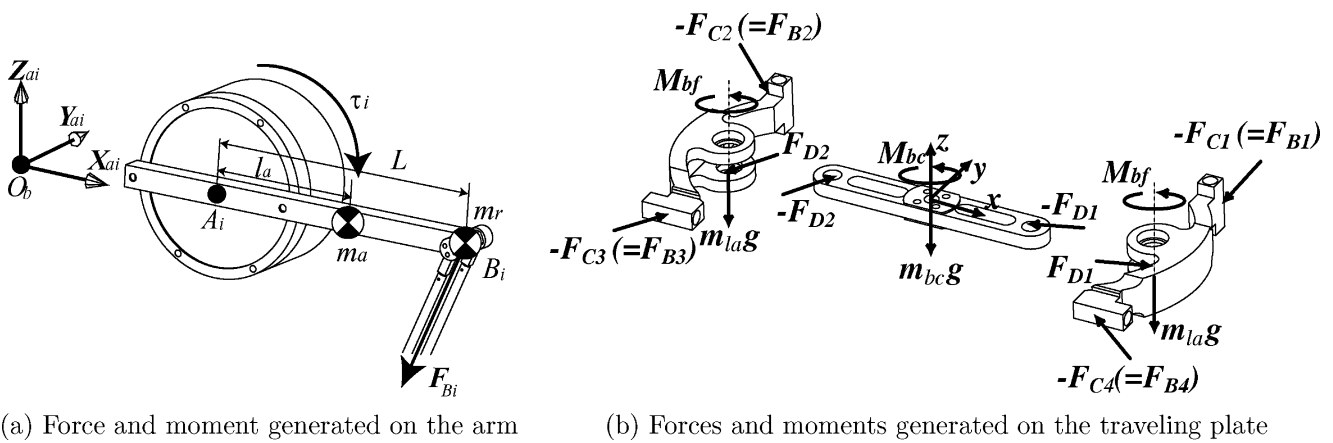$$\boldsymbol{F}_t = m_{bc}(\ddot{\boldsymbol{o}}_t + \boldsymbol{g}) + m_{la}(\ddot{\boldsymbol{d}}_1 + \ddot{\boldsymbol{d}}_2 + 2\boldsymbol{g}) + \boldsymbol{F}_{\text{ext}}, \quad (17)$$

$$N_{tz} = \left\{ \boldsymbol{I}_t\dot{\boldsymbol{\omega}}_t + \boldsymbol{\omega}_t \times (\boldsymbol{I}_t\boldsymbol{\omega}_t) + m_{la}\sum_{i=1}^{2}\overrightarrow{O_tD_i} \right.$$
$$\left. \times (\ddot{\boldsymbol{d}}_i + \boldsymbol{g}) + N_{\text{ext}} \right\} \cdot \boldsymbol{Z}_t, \quad (18)$$

where m_{bc}, m_{la} are the masses of the central bar and lateral bar (see Fig. 14-(b)), $\boldsymbol{o}_t$, $\boldsymbol{d}_1$, and $\boldsymbol{d}_2$ are the three-dimensional position vector of the points O_t, D_1, and D_2 (see Fig. 8), respectively, $\boldsymbol{I}_t$ is the inertia tensor of the traveling plate, and $\boldsymbol{F}_{\text{ext}}$, $\boldsymbol{N}_{\text{ext}}$ are the external force and moment vectors.

Here, $\boldsymbol{\omega}_t$ is the angular velocity vector of the traveling plate and is given by

$$\boldsymbol{\omega}_t = \dot{\alpha}\boldsymbol{Z}_t. \quad (19)$$

$\boldsymbol{d}_i$, $\dot{\boldsymbol{d}}_i$, and $\ddot{\boldsymbol{d}}_i$ are expressed using $\boldsymbol{o}_t$, $\boldsymbol{\omega}_t$, and $\overrightarrow{O_tD_i}$ as follows:

$$\boldsymbol{d}_i = \boldsymbol{o}_t + \overrightarrow{O_tD_i}, \quad (20)$$

$$\dot{\boldsymbol{d}}_i = \dot{\boldsymbol{o}}_t + \boldsymbol{\omega}_t \times \overrightarrow{O_tD_i} = \dot{\boldsymbol{o}}_t + \dot{\alpha}\boldsymbol{Z}_t \times \overrightarrow{O_tD_i}, \quad (21)$$

$$\ddot{\boldsymbol{d}}_i = \ddot{\boldsymbol{o}}_t + \dot{\boldsymbol{\omega}}_t \times \overrightarrow{O_tD_i} + \boldsymbol{\omega}_t \times (\boldsymbol{\omega}_t \times \overrightarrow{O_tD_i})$$
$$= \ddot{\boldsymbol{o}}_t + \ddot{\alpha}\boldsymbol{Z}_t \times \overrightarrow{O_tD_i} - \dot{\alpha}^2\overrightarrow{O_tD_i}. \quad (22)$$

Substituting Eq. (22) into Eq. (17) and considering that $\overrightarrow{O_tD_2} = -\overrightarrow{O_tD_1}$, Eq. (17) is simplified as follows:

$$\boldsymbol{F}_t = (m_{bc} + 2m_{la})(\ddot{\boldsymbol{o}}_t + \boldsymbol{g}) + \boldsymbol{F}_{\text{ext}}. \quad (23)$$

Scalar triple products in Eq. (18) are simplified as follows:

$$(\boldsymbol{\omega}_t \times (\boldsymbol{I}_t\boldsymbol{\omega}_t)) \cdot \boldsymbol{Z}_t = (\boldsymbol{Z}_t \times \boldsymbol{\omega}_t) \cdot (\boldsymbol{I}_t\boldsymbol{\omega}_t) = 0,$$

$$\left(\overrightarrow{O_tD_i} \times \boldsymbol{g}\right) \cdot \boldsymbol{Z}_t = (\boldsymbol{g} \times \boldsymbol{Z}_t) \cdot \overrightarrow{O_tD_i} = 0.$$

Therefore, Eq. (18) can be rewritten as follows:

$$N_{tz} = \left(\boldsymbol{Z}_t^T\boldsymbol{I}_t\boldsymbol{Z}_t + 2m_{la}h^2\right)\ddot{\alpha} + N_{\text{ext}_z} \quad (24)$$
$$N_{\text{ext}_z} = \boldsymbol{N}_{\text{ext}} \cdot \boldsymbol{Z}_t$$

Substituting Eq. (23) and Eq. (25) into Eq. (15), the following equation is obtained:

$$\boldsymbol{n} = \boldsymbol{J}^T \begin{bmatrix} \boldsymbol{F}_t \\ N_{tz} \end{bmatrix}$$
$$= \boldsymbol{J}^T \begin{bmatrix} (m_{bc} + 2m_{la})\boldsymbol{E}_{3\times3} & 0 \\ \boldsymbol{0}_{1\times3} & \boldsymbol{Z}_t^T\boldsymbol{I}_t\boldsymbol{Z}_t + 2m_{la}h^2 \end{bmatrix} \begin{bmatrix} \ddot{\boldsymbol{o}}_t \\ \ddot{\alpha} \end{bmatrix}$$
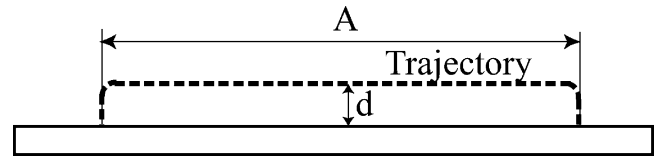
Fig. 15. Specification of the adept motion.

$$+ \boldsymbol{J}^T \begin{bmatrix} (m_{bc} + 2m_{la})\boldsymbol{g} \\ 0 \end{bmatrix} + \boldsymbol{J}^T \begin{bmatrix} \boldsymbol{F}_{\text{ext}} \\ N_{\text{ext}_z} \end{bmatrix}$$
$$= \boldsymbol{J}^T\overline{\boldsymbol{M}}\ddot{\boldsymbol{p}} + \boldsymbol{J}^T\overline{\boldsymbol{G}} + \boldsymbol{J}^T \begin{bmatrix} \boldsymbol{F}_{\text{ext}} \\ N_{\text{ext}_z} \end{bmatrix}, \quad (25)$$

where $\boldsymbol{E}_{k\times k}$ is a $k \times k$ identity matrix. Differentiating Eq. (10), $\ddot{\boldsymbol{p}}$ can be expressed as follows:

$$\ddot{\boldsymbol{p}} = \boldsymbol{J}\ddot{\boldsymbol{\theta}} + \dot{\boldsymbol{J}}\dot{\boldsymbol{\theta}} \quad (26)$$

Substituting Eq. (26) and Eq. (25) into Eq. (16), the equation of motion is obtained as follows:

$$\boldsymbol{\tau} = \boldsymbol{M}(\boldsymbol{\theta})\ddot{\boldsymbol{\theta}} + \boldsymbol{h}(\dot{\boldsymbol{\theta}}, \boldsymbol{\theta}) + \boldsymbol{G}(\boldsymbol{\theta}) + \boldsymbol{V}(\dot{\boldsymbol{\theta}}) + \boldsymbol{J}^T \begin{bmatrix} \boldsymbol{F}_{\text{ext}} \\ N_{\text{ext}_z} \end{bmatrix}, \quad (27)$$

where

$$\boldsymbol{M}(\boldsymbol{\theta}) = (I_a + m_rL^2 + I_m)\boldsymbol{E}_{4\times4} + \boldsymbol{J}^T\overline{\boldsymbol{M}}\boldsymbol{J},$$
$$\boldsymbol{h}(\dot{\boldsymbol{\theta}}, \boldsymbol{\theta}) = \boldsymbol{J}^T\overline{\boldsymbol{M}}\dot{\boldsymbol{J}}\dot{\boldsymbol{\theta}},$$
$$\boldsymbol{G}(\boldsymbol{\theta}) = \boldsymbol{J}^T\overline{\boldsymbol{G}} + (m_ala + m_rL)g \begin{bmatrix} 0 \\ 0 \\ \cos\theta_3 \\ \cos\theta_4 \end{bmatrix}.$$

6. Evaluation of the Simplified Model
In order to evaluate the simplified model, simulations are performed.

6.1. Adept motion
The Adept motion is chosen as a benchmark test to evaluate the capability for quickness of the H4 robot. Figure 15 illustrates a rough scheme of the Adept motion. The dotted line in the figure represents the trajectory along which the endpoint of the robot should track. There are no specifications on the corner radius, travel distance A and height d of the trajectory. In the evaluation experiment, the travel distance and height are specified as $A = 0.300\,\text{m}$ and $d = 0.025\,\text{m}$, respectively. Both ends of the trajectory are set at $(\,x \quad y \quad z\,) = (\,-0.15 \quad 0.0 \quad -0.52\,)$ and $(\,0.15 \quad 0.0 \quad -0.52\,)\,\text{m}$, respectively.

6.2. Simulation results
The traveling plate of the H4 robot is moved along the specified trajectory to and from both of the ends. The round-trip cycle time is set to 0.84 s. A short wait (0.02 s) is inserted at both ends of the trajectory in order to simulate a pick-and-place operation. It is assumed that the external forces and moment are not applied to the traveling plate during the

(a) Motor 1   (b) Motor 2

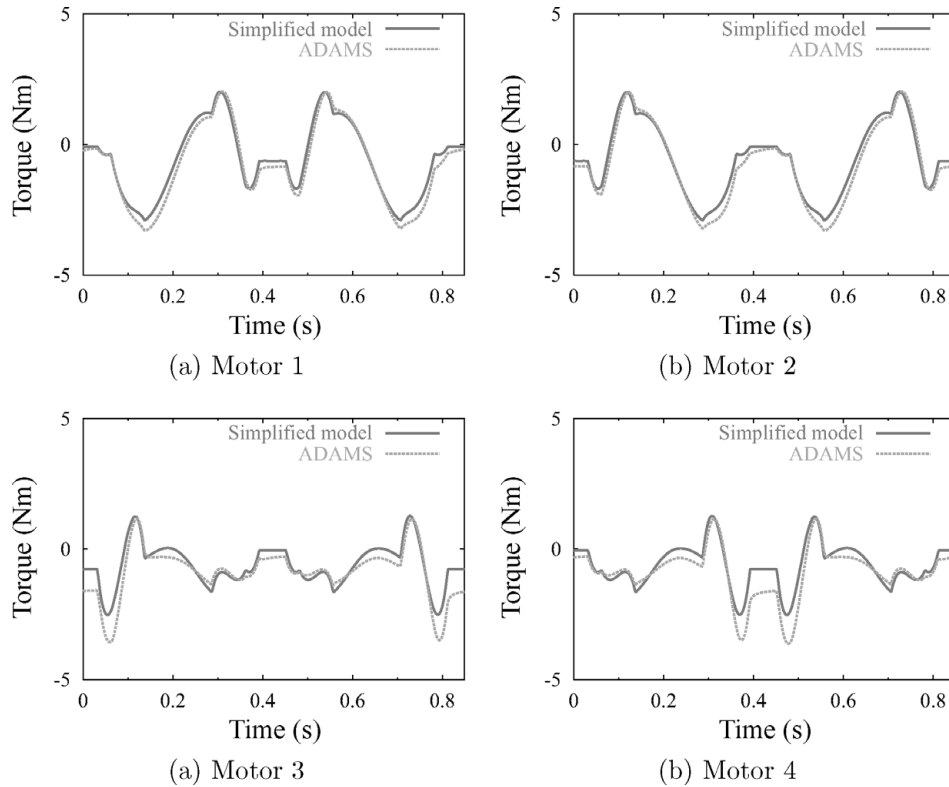(a) Motor 3   (b) Motor 4

Fig. 16. Motor torques (round-trip cycle time is 0.84 s).

motion, and the viscous frictions are small enough to be ignored.

The simulation results are plotted in Fig. 16. The solid lines in Fig. 16 are the motor torques calculated from the simplified model (27) when the Adept motion trajectory is given, while the dashed lines are the torques derived from an engineering analysis software package ADAMS™ supplied by MSC software corporation. ADAMS computes the full dynamics of the H4 robot based on the CAD model.

Slight differences can be seen between the torques computed from the simplified model (solid lines) and torques derived from ADAMS (dashed lines). The average error rate of those torques with respect to ADAMS results is 24.5%. From the results shown in Fig. 16, it is concluded that the simplified model has enough accuracy in the computation of the inverse dynamics of the H4 robot.

7. Evaluation of the Performance

The quickness of the H4 robot is evaluated by performing experiments. Three different controllers are applied and evaluated: (i) PD (proportional-derivative) controller, (ii) PD controller with velocity feed-forward, and (iii) dynamic compensation controller.

7.1. Velocity feedback controller

Since the motor drivers of the H4 robot provide the hardware velocity servo, the torques cannot be directly commanded to the motor drivers. Therefore, the torque command has to be converted into the velocity command. At first the hardware velocity servo is modeled as follows:

$$\boldsymbol{\tau} = K_v(\dot{\boldsymbol{\theta}}_{com} - \dot{\boldsymbol{\theta}}), \qquad (28)$$

where $\boldsymbol{\tau}$, $\dot{\boldsymbol{\theta}}_{com}$, and $\dot{\boldsymbol{\theta}}$ denote the motor torque vector, the velocity command vector, and the motor velocity vector, respectively. K_v is the velocity feedback gain of the motor driver. User gives $\dot{\boldsymbol{\theta}}_{com}$ as a control input to the motor drivers.

As described above, three controllers, (i) PD controller, (ii) PD controller with velocity feed-forward, and (iii) dynamic compensation controller are tested. These controllers are developed to meet the velocity servo motor drivers.

7.2. PD controller

In the PD controller, the velocity command vector $\dot{\boldsymbol{\theta}}_{com}$ in Eq. (28) is computed as

$$\dot{\boldsymbol{\theta}}_{com} = K_p(\boldsymbol{\theta}_d - \boldsymbol{\theta}) + K_d(\dot{\boldsymbol{\theta}}_d - \dot{\boldsymbol{\theta}}), \qquad (29)$$

where $\boldsymbol{\theta}_d$ denotes the desired motor angle vector, $\boldsymbol{\theta}$ is the motor angle vector measured by the resolvers.

7.3. PD controller with velocity feed-forward

In the PD controller with velocity feed-forward, the velocity command vector $\dot{\boldsymbol{\theta}}_{com}$ is computed as:

$$\dot{\boldsymbol{\theta}}_{com} = \dot{\boldsymbol{\theta}}_{ff} + K_p(\boldsymbol{\theta}_d - \boldsymbol{\theta}) + K_d(\dot{\boldsymbol{\theta}}_d - \dot{\boldsymbol{\theta}}), \qquad (30)$$

where $\dot{\boldsymbol{\theta}}_{ff}$ is a feed-forward term to compensate the servo delay, and given as

$$\dot{\boldsymbol{\theta}}_{ff}(t) = \dot{\boldsymbol{\theta}}_d(t + \Delta T), \qquad (31)$$

where ΔT is the sampling period set to be 2 ms.

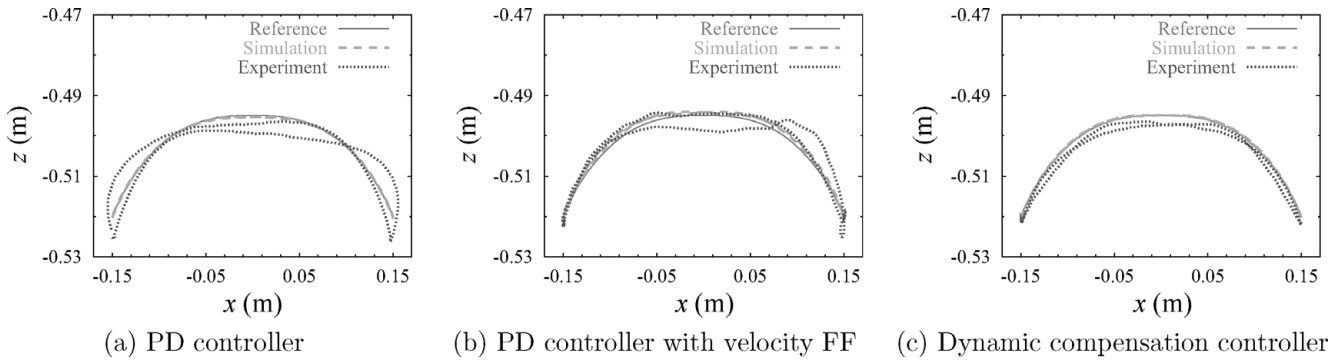| (a) PD controller | (b) PD controller with velocity FF | (c) Dynamic compensation controller |

Fig. 17. Trajectories in x–z plane (round-trip cycle time is 0.48 s).

7.4. Dynamic compensation controller
In the dynamic compensation controller, the velocity command vector $\dot{\theta}_{com}$ is given as:

$$\dot{\theta}_{com} = K_v^{-1}\tau_d + \dot{\theta}_{ff} + K_p(\theta_d - \theta) + K_d(\dot{\theta}_d - \dot{\theta}), \quad (32)$$

where τ_d denotes the torque vector calculated from the simplified model Eq. (27).

7.5. Simulation and experimentation results
The simulations and experiments are performed using the three different controllers: PD controller, PD controller with velocity feed-forward, and dynamic compensation controller. The Adept motion is used for evaluation. The round-trip cycle time is set to 0.48 s. As is the case with the evaluation of the simplified model, a short wait (0.02 s) is inserted at both ends of the trajectory.

In the simulations and experiments, the control gains, K_p, K_d, and K_v are set to 200 s^{-1}, 2.0 and 11 Nms/rad, respectively.

The resultant trajectories of the traveling plate in x–z plane are plotted in Fig. 17. Figures 18 and 19 depict the torques produced by the motors 1 and 3, respectively. The dynamic compensation τ_d is superimposed on the Figures 18(c) and 19(c) for reference.

As clearly seen in Fig. 17, the traveling plate cannot precisely track the reference trajectory when the conventional PD controller is applied. Although the velocity feed-forward contributes to reducing the tracking error, the tracking error remains. Among the three controllers, the dynamic compensation controller shows the best performance. Figures 20– 23 present joint trajectories of the motors 1 and 3, and the traveling plate trajectories against the time along X_t and Z_t axes, respectively.
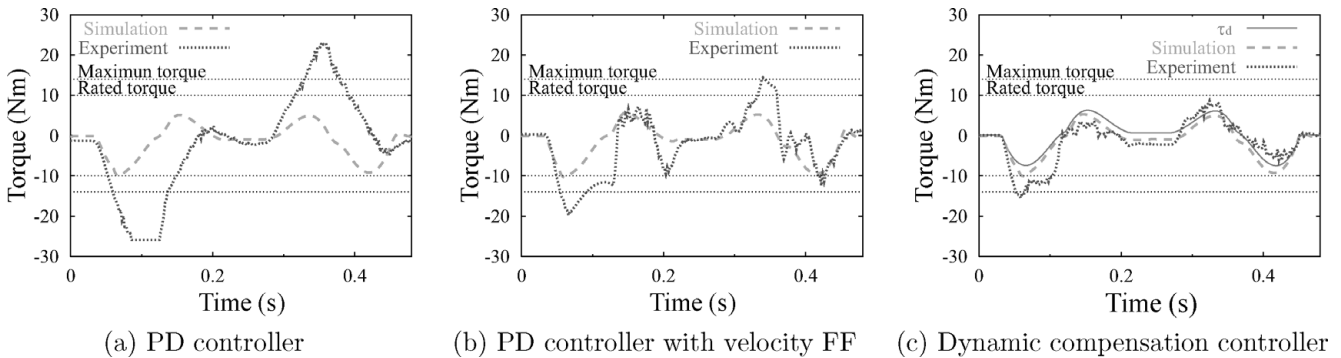

| (a) PD controller | (b) PD controller with velocity FF | (c) Dynamic compensation controller |

Fig. 18. Generated torque of motor 1 (round-trip cycle time is 0.48 s).

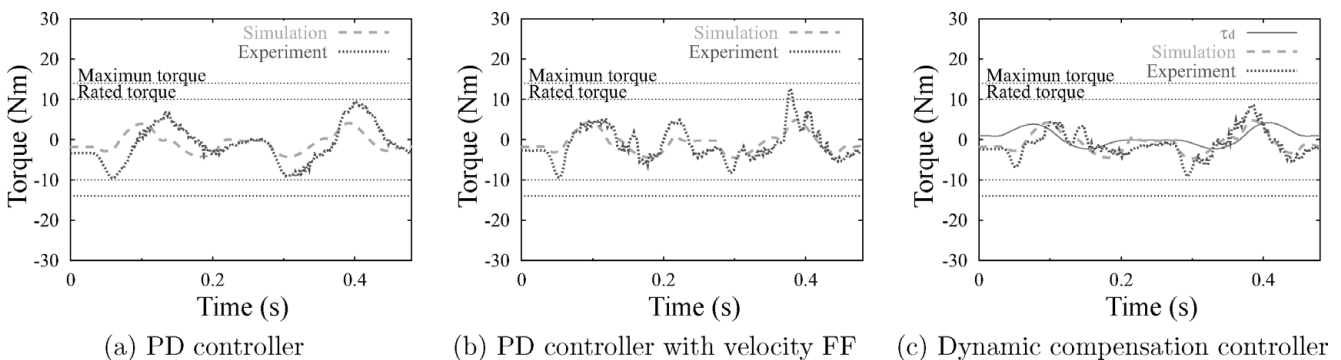| (a) PD controller | (b) PD controller with velocity FF | (c) Dynamic compensation controller |

Fig. 19. Generated torque of motor 3 (round-trip cycle time is 0.48 s).
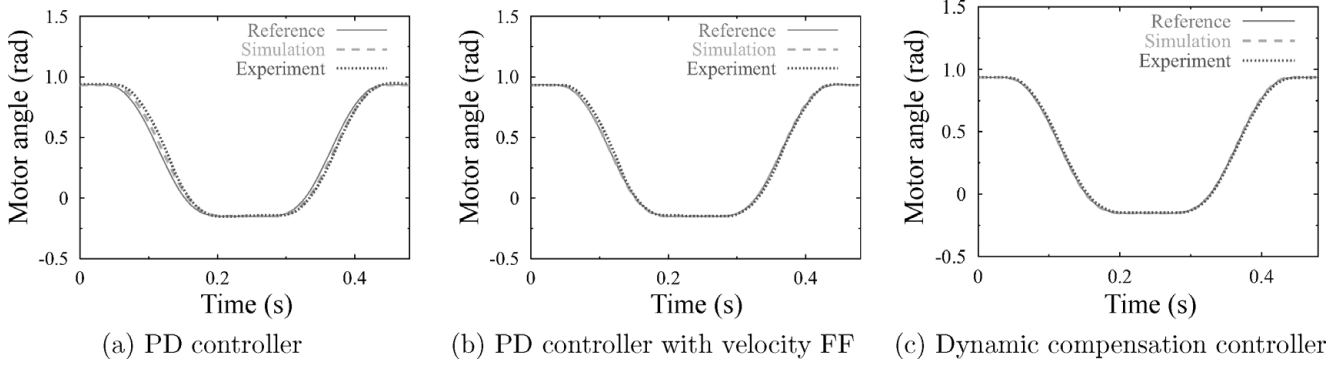
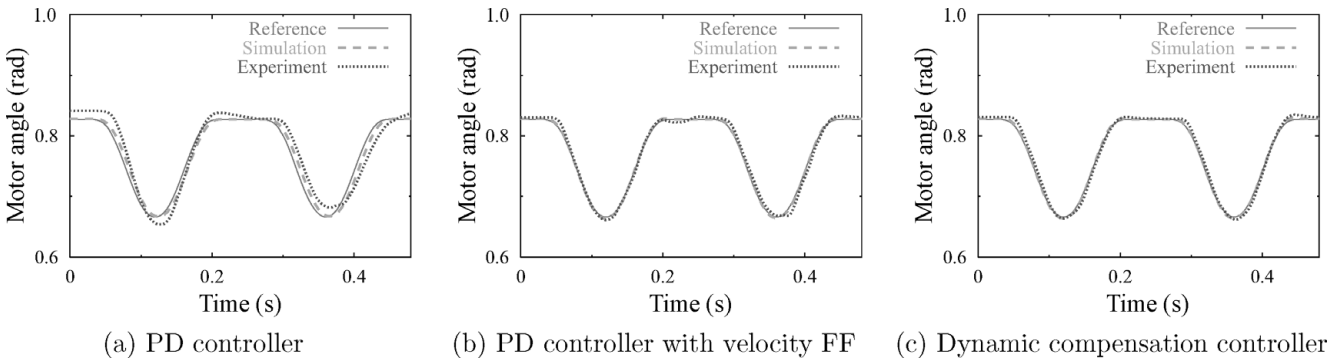Fig. 20. Response of motor 1 (round-trip cycle time is 0.48 s).

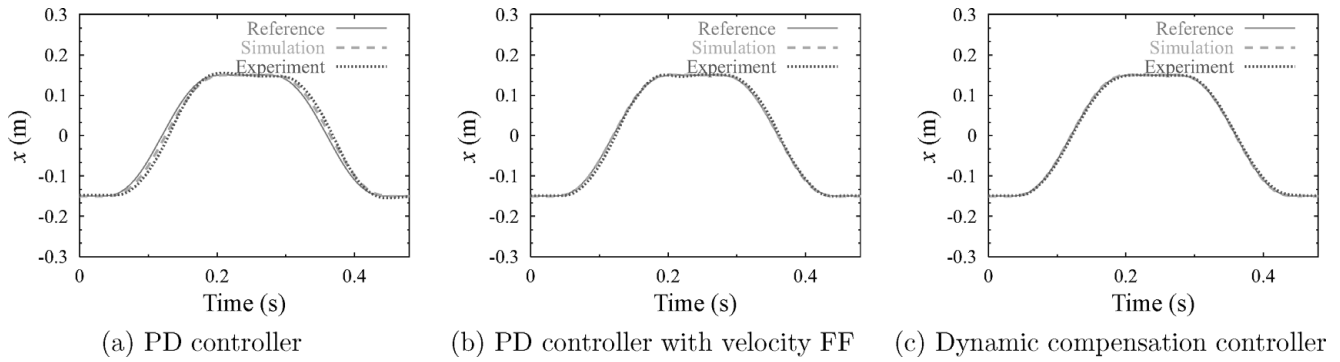Fig. 21. Response of motor 3 (round-trip cycle time is 0.48 s).

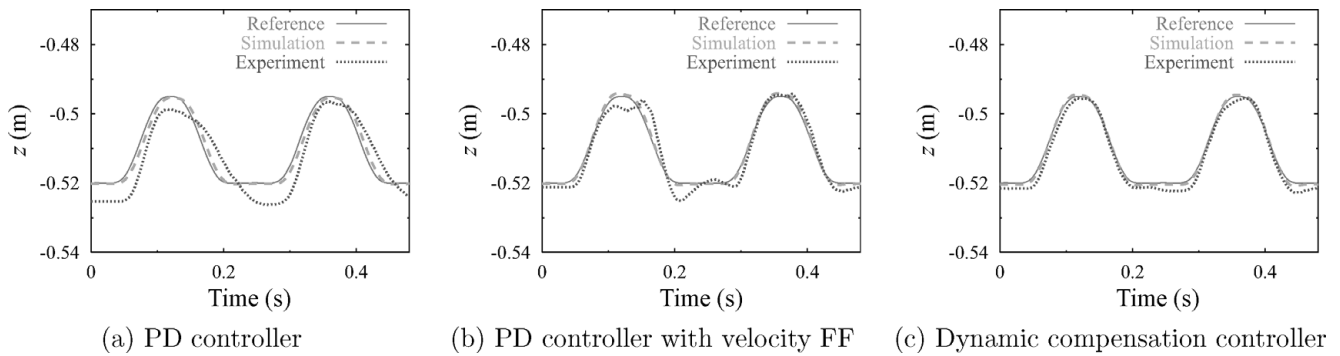Fig. 22. $t–x$ profile (round-trip cycle time is 0.48 s).

Fig. 23. $t–z$ profile (round-trip cycle time is 0.48 s).

In order to track the given Adept motion trajectory within the specified round-trip cycle time (0.48 s), the robot must move very quickly. The average speed of the end-point is 1.458 m/s (0.7 m/0.48 s). Figure 17(c) shows that the H4 robot achieves such very quick motion without large tracking error when the dynamic compensation controller is applied.

Figures 18 and 19 show that the dynamic compensation controller contributes to reducing the torque, as well as to reducing the tracking error.

8. Conclusion
This paper presents the design, kinematics, and controllers of the newly developed parallel robot H4. The H4 robot provides full parallel 4-DOF: three translations and one rotation. Compared with the conventional parallel-serial hybrid design (e.g. DELTA + one rotation), the full parallel H4 robot has advantages in quickness, rigidity, simplicity in mechanism, and high accuracy. Inverse kinematics solution and Jacobian matrices for the H4 robot are given. The manipulability ellipsoid and measure of the H4 are addressed in order to confirm their manipulating ability which has good performance along x- and y-axis. A simplified dynamic model is proposed for H4 robot. In order to evaluate the accuracy of the simplified model, the inverse dynamic solution derived from the simplified model is compared with the solution computed by ADAMS software which computes full dynamics based on the CAD model. The comparison shows that the simplified model has enough accuracy in computation in the inverse dynamics.

Three controllers are developed and tested: PD controller, PD controller with velocity feed-forward, and dynamic compensation controller. The Adept motion is chosen as a benchmark test to evaluate the controllers and the performance of the H4 robot. When a very quick motion (round-trip cycle time is 0.48 s) is tested, PD controller yields significant tracking error. A feed-forward term contributes to reduce the tracking error, however, the error remains and the tracking result is not satisfactory. The dynamic compensation controller drastically improves the tracking error and brings best result. The result shows the performance of quickness of the H4 robot, too. Taking advantage of the quickness, the H4 robot will contribute to improve the take time in various applications.

References
1. T. Arai, K. Cleary, T. Nakamura, H. Adachi and K. Homma, "Design, Analysis and Construction of a Prototype Parallel Link Manipulator," *Proceedings of IEEE/RSJ International Conferance on Intelligent Robots and Systems*, Ibaraki, Japan (1990) pp. 205–212.
2. T. Arai, R. Stoughton, K. Homma, H. Adachi and T. Nakamura, "Development of a Parallel Link Manipulator," *Proceedings of the 5th International Conference on Advanced Robotics*, Pise (1991) vol. 1, pp. 839–844.
3. H. B. Choi, O. Company, F. Pierrot, A. Konno, T. Shibukawa, K. Abe, D. Sato and M. Uchiyama, "Design and dynamic simulation of a novel 4-DOFs parallel robot H4," *Trans. JSME (Ser. C, Japanese)* **70**(691), 798–803 (2004).
4. H. B. Choi, A. Konno and M. Uchiyama, "Closed-Form Solutions for the Forward Kinematics of a 4-DOFs Parallel Robot H4," *Proceedings of IEEE/RSJ International Conference on Intelligent Robots and Systems*, Las Vegas, USA (2003a) pp. 3312–3317.
5. H. B. Choi, A. Konno and M. Uchiyama, " Singularity Analysis of a Novel 4-DOFs Parallel Robot H4 by Using Screw Theory," *Proceedings of the DETC'03 ASME 2003 Design Engineering Technical Conferences and Computers and Information in Engineering Conference*, Chicago, USA (2003b) Number DAC–48704, pp. 1–9.
6. R. Clavel, "Delta, a Fast Robot with Parallel Geometry," *Eighteenth International Symposium on Industrial Robot*, Lausanne, Switzerland (1998) pp. 91–100.
7. V. E. Gough, "Contribution to Discussion to Papers on Research in Automobile Stability and Control and in Tire Performance," *Proceedings of the Automobile Division of the Institution of Mechanical Engineers* (1956–1957).
8. D. Kim, K. Abe, T. Shitashimizu, D. Sato and M. Uchiyama, "Design of a ball joint and rod with large swing angle for a parallel robot in which epoxy-type bond is used," *Japan Soc. Mech. Eng.* **66**(676), 3666–3672 (2002).
9. J. Kim, J. Hwang, J. Kim, C. C. Iurascu, F. C. Park and Y. Cho, "Eclipse-ll: A new parallel mechanism enabling continuous 360-degree spinning plus three-axis translational motions," *IEEE Trans. Robot. Autom.* **18**(3), 367–373 (2002).
10. J. Kim, F. C. Park, S. J. Ryu, J. Kim, J. Hwang, C. Park and C. Iurascu, "Design and analysis of a redundantly actuated parallel mechanism for rapid machining," *IEEE Trans. Robot. Autom.* **17**(4), 423–434 (2001).
11. J. P. Merlet. *Parallel Robots* (Kluwer Academic Publishers, 2000).
12. F. Pierrot and O. Company, "H4: A New Family of 4-DOF Parallel Robots," *Proceedings of the IEEE/ASME International Conference on Advanced Intelligent Mechatronics*, Atlanta, USA (1999) pp. 508–513.
13. F. Pierrot, F. Marquet, O. Company and T. Gil, "H4 Parallel Robot: Modeling and Preliminary Experiment," *Proceedings of IEEE International Conference on Robotics and Automation*, Seoul, Korea (2001) pp. 3256–3261.
14. F. Pierrot, M. Uchiyama, P. Dauchez and A. Fournier, "A new design of a 6-dof parallel robot," *J. Robot. Mechatronics* **2**(4), 308–315 (1990).
15. D. Stewart, "A Platform with Six Degrees of Freedom," *Proceedings of the Institution of Mechanical Engineers* **180**(15), 371–386 (1965–1966).
16. L. W. Tsai, "*Robot Analysis* (John Wiley Sons, 1999).
17. M. Uchiyama, K. Iimura, F. Pierrot, P. Dauchez, K. Unno and O. Toyama, "A New Design of a Very Fast 6-DOF Parallel Robot," *Proceedings of the 23rd International Symposium on Industrial Robots*, Barcelona, Spain (1992) pp. 771–776.
18. M. Uchiyama, K. Masukawa and T. Sadotomo, "Experiment on Dynamic Control of a Hexa-type Parallel Robot. *Proceedings of the 1st World Automation Congress*, Hawaii, USA (1994) Vol. **2**, pp. 281–286.
19. T. Yoshikawa, "Dynamic manipulability of robot manipulators," *J. Robot. Syst.* **2**(1), 113–124 (1985a).
20. T. Yoshikawa, "Manipulability of robotic mechanism," *Int. J. Robot. Res.* **4**(2), 3–9 (1985b).